Nano Research
2019, 12(5): 1093–1098

ISSN 1998-0124 CN 11-5974/O4
https://doi.org/10.1007/s12274-019-2352-5

Research Article

Mn_3O_4 nanoparticles@reduced graphene oxide composite: An efficient electrocatalyst for artificial N_2 fixation to NH_3 at ambient conditions

Hong Huang[1,§], Feng Gong[3,§], Yuan Wang[1], Huanbo Wang[2], Xiufeng Wu[1,4], Wenbo Lu[4], Runbo Zhao[1], Hongyu Chen[1], Xifeng Shi[5], Abdullah M. Asiri[6], Tingshuai Li[3], Qian Liu[3], and Xuping Sun[1] (✉)

[1] *Institute of Fundamental and Frontier Sciences, University of Electronic Science and Technology of China, Chengdu 610054, China*
[2] *School of Environment and Resource, Southwest University of Science and Technology, Mianyang 621010, China*
[3] *School of Materials and Energy, University of Electronic Science and Technology of China, Chengdu 611731, China*
[4] *Key Laboratory of Magnetic Molecules and Magnetic Information Materials (Ministry of Education), School of Chemistry and Material Science, Shanxi Normal University, Linfen 041004, China*
[5] *College of Chemistry, Chemical Engineering and Materials Science, Shandong Normal University, Jinan 250014, China*
[6] *Chemistry Department, Faculty of Science & Center of Excellence for Advanced Materials Research, King Abdulaziz University, P.O. Box 80203, Jeddah 21589, Saudi Arabia*
§ *Hong Huang and Feng Gong contributed equally to this work.*

Received: 3 January 2019 / **Revised:** 1 February 2019 / **Accepted:** 18 February 2019

ABSTRACT

Currently, industrial-scale NH_3 production almost relies on energy-intensive Haber-Bosch process from atmospheric N_2 with large amount of CO_2 emission, while low-cost and high-efficient catalysts are demanded for the N_2 reduction reaction (NRR). In this study, Mn_3O_4 nanoparticles@reduced graphene oxide (Mn_3O_4@rGO) composite is reported as an efficient NRR electrocatalyst with excellent selectivity for NH_3 formation. In 0.1 M Na_2SO_4 solution, such catalyst obtains a NH_3 yield of 17.4 $\mu g \cdot h^{-1} \cdot mg^{-1}_{cat.}$ and a Faradaic efficiency of 3.52% at −0.85 V vs. reversible hydrogen electrode. Notably, it also shows high electrochemical stability during electrolysis process. Density functional theory (DFT) calculations also demonstrate that the (112) planes of Mn_3O_4 possess superior NRR activity.

KEYWORDS

Mn_3O_4@rGO composite, electrocatalyst, NH_3 synthesis, N_2 reduction reaction, ambient conditions

1 Introduction

NH_3 is a significant substance to produce agricultural fertilizers, plastic and pharmaceuticals, and it is also a fascinating carbon-free energy carrier with high energy density [1–4]. Although N_2 is the most abundant molecule in the atmosphere, the thermodynamic stability and strong N≡N triple bond (941 $kJ \cdot mol^{-1}$) make it chemically inert, and the N_2 reduction into NH_3 is an extremely difficult process. In Haber-Bosch process, this kinetic limitation is overcome by using high temperature and elevated pressure with large amount of CO_2 emission [5]. So, it is imperative to develop an environmentally friendly process for sustainable N_2 fixation.

Electrochemical NH_3 synthesis is a promising candidate for artificial N_2 fixation at ambient conditions due to its environmental-friendly, convenient, and low-cost characteristics [6–8]. However, efficient catalysts are still needed for N_2 reduction reaction (NRR). Noble-metal catalysts exhibit favorable NRR activity [9–11], but the high cost restricts their widespread use. It is thus highly desired to design and develop non-precious metal alternatives [12–23]. As an earth-abundant transition metal oxide, Mn_3O_4 shows many merits, such as low cost, natural abundance, and environmental friendliness. Our recent work suggests Mn_3O_4 nanocube is an efficient catalyst for NRR [24]. Unfortunately, Mn_3O_4 has poor electrical conductivity (10^{-7}–10^{-8} $S \cdot cm^{-1}$) [25, 26]. Reduced graphene oxide (rGO) is deemed to be an attractive carbon material due to its good electrochemical stability, high surface area, and superior mechanical as well as electronic conductivity [27–30]. Study indicates that rGO anchored Mn_3O_4 composite exhibits improved conductivity and large active surface area [31], providing us a possible catalyst for electrochemical N_2 reduction, which, however, has not been explored before.

In this study, for the first time, we present our recent finding that Mn_3O_4 nanoparticles@rGO (Mn_3O_4@rGO) composite acts as an efficient catalyst for electrochemical NRR (Scheme 1). In 0.1 M Na_2SO_4, such Mn_3O_4@rGO catalyst exhibits a Faradaic efficiency (FE) of 3.52% and a NH_3 yield of 17.4 $\mu g\ h^{-1} \cdot mg^{-1}_{cat.}$ at −0.85 V vs. reversible hydrogen electrode (RHE) with excellent selectivity. Moreover, it also shows high electrochemical stability for electrolysis process. Density functional theory (DFT) calculations suggest the superior NRR activity on the (112) planes of Mn_3O_4.

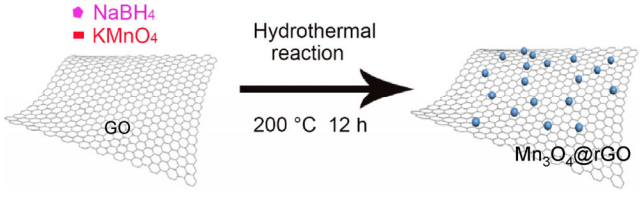

Scheme 1 A schematic diagram to illustrate the preparation process of Mn_3O_4@rGO.

Address correspondence to xpsun@uestc.edu.cn

2 Experimental

2.1 Materials

GO powder was purchased from Aladdin Ltd. (Shanghai, China). $KMnO_4$ and $NaBH_4$ (purity, 99.9%) were bought from Tianjing Fuchen Chemical Reagent Factory. Nafion (5 wt.%) was purchased from Sigma-Aldrich Chemical Reagent Co., Ltd. All chemicals were used as received without further purification. Deionized water was used throughout the experiments.

2.2 Preparation of Mn_3O_4@rGO

Mn_3O_4@rGO composite was synthesized as described below. 1 g·L^{-1} homogeneous GO suspension was prepared by ultrasonication of GO (50 mg) in doubly distilled water (50 mL) for 2 h. Then, 10 mM of $KMnO_4$ solution (50 mL) was added, and the mixture solution was vigorously stirred and completely dissolved. Subsequently, 0.38 g of $NaBH_4$ aqueous solution (100 mL) was added to the above solution mixture with stirring. The solution was transferred into 50 mL stainless steel autoclaves. The autoclaves were sealed and maintained at 200 °C for 12 h. The autoclaves cooled to room temperature naturally. Final precipitate was collected and rinsed thoroughly with doubly distilled water and ethanol several times, then dried in a vacuum oven overnight at 60 °C. For comparison, pure Mn_3O_4 and rGO were also prepared by a similar procedure.

2.3 Preparation of Mn_3O_4@rGO carbon paper electrode (Mn_3O_4@rGO/CP)

5 mg Mn_3O_4@rGO composite and 20 μL of Nafion solution (5 wt.%) were dispersed in 980 μL mixed solution containing ethanol and H_2O (V:V = 1:1) by 3 h sonication to form a homogeneous ink. Then 30 μL catalyst ink was loaded on a piece of 1 cm × 1 cm carbon paper.

2.4 Calculation of ECSA

Electrochemical capacitance measurements were used to determine the active surface area of Mn_3O_4@rGO [32]. Cyclic voltammograms (CVs) were performed at the scanning rates from 20–100 mV·s^{-1}. The specific capacitance can be converted into the electrochemical surface areas (ECSA) using the specific capacitance value for a flat standard with 1 cm^2 of real surface area. The specific capacitance for a flat surface is generally found to be in the range of 20–60 μF·cm^{-2} [33, 34].

ECSA calculation is listed as following equation

$$A\frac{\text{Mn}_3\text{O}_4\text{@rGO}}{\text{ECSA}} = \frac{\text{Slope}\ \mu\text{F}\cdot\text{cm}^{-2}}{60\ \mu\text{F}\cdot\text{cm}^{-2}\ \text{per}\ \text{cm}^2_{\text{ECSA}}} \quad (1)$$

2.5 Determination of NH_3

Concentration of produced NH_3 was spectrophotometrically determined by the indophenol blue method [35]. Typically, a 4 mL post-tested solution was taken from the electrochemical cathodic chamber. Then, 50 μL of oxidizing solution (NaClO (ρ_{Cl} = 4–4.9) and 0.75 M NaOH), 500 μL of coloring solution (0.4 M $C_7H_5O_3Na$ and 0.32M NaOH) and 50 μL of catalyst solution (0.1 g $Na_2[Fe(CN)_5NO]2H_2O$ diluted to 10 mL with deionized water) were added sequentially to the sample solution. After 2 h, the ultraviolet–visible (UV–vis) absorption spectrum was measured using the UV–vis spectrophotometer at a wavelength of 655 nm. The concentration-absorbance curves were calibrated using standard NH_4^+ solution with a serious of concentrations from 0 to 0.225 μg·mL^{-1}. The fitting curve (y = 0.516x + 0.024, R^2 = 0.999) shows good linear relation of absorbance value with NH_4^+ concentration.

2.6 Determination of N_2H_4

The N_2H_4 presented in the electrolyte was estimated by the method of Watt and Chrisp [36]. A mixed solution of 5.99 g $C_9H_{11}NO$, 30 mL HCl, and 300 mL ethanol was used as a color reagent. Calibration curve was plotted as follow: (1) preparing a series of reference solutions; (2) adding 5 mL above prepared color reagent and stirring 20 min at room temperature; (3) the absorbance of the resulting solution was measured at 455 nm, and the yields of N_2H_4 were estimated from a standard curve using 5 mL residual electrolyte and 5 mL color reagent. Absolute calibration of this method was achieved using N_2H_4 solutions of known concentration as standards, and the fitting curve shows good linear relation of absorbance with N_2H_4 concentration (y = 0.486x + 0.030, R^2 = 0.999).

2.7 Determination of FE

The FE for N_2 reduction was defined as the amount of electric charges used for synthesizing NH_3 divided by the amount of total charges passed through the electrodes during the electrolysis. The total amount of NH_3 produced was measured using colorimetric methods. Assuming three electrons were needed to produce one NH_3 molecule, calculations of NH_3 yield and FE: NH_3 formation rate was calculated as follows

$$\text{NH}_3\ \text{yield} = [\text{NH}_4^+] \times V / (m_{\text{cat.}} \times t) \quad (2)$$

FE could be calculated using the following equation

$$\text{FE} = 3 \times F \times [\text{NH}_4^+] \times V / (18 \times Q) \quad (3)$$

where $[NH_4^+]$ is the measured NH_4^+ ion concentration; V is the volume of the cathodic reaction electrolyte; t is the potential applied time; m is the loaded quality of catalyst; F is the Faraday constant; and Q is the quantity of applied electricity.

FE for H_2 was calculated according to following equation

$$\text{FE} = 2 \times F \times n / Q \quad (4)$$

where F is the Faraday constant; n is the experimentally produced H_2 (mol), and Q is the quantity of applied electricity.

2.8 Characterizations and electrochemical tests

X-ray diffraction (XRD) data were collected on a Rigaku X-ray diffractometer equipped with a Cu Kα radiation source. Raman spectroscopy of the products was obtained on LabRAM HR. Scanning electron microscopy (SEM) images were obtained on a Hitachi S-4800 field emission scanning electron microscope at an accelerating voltage of 20 kV. Transmission electron microscopy (TEM) measurements were performed on a Zeiss Libra 200FE transmission electron microscope operated at 200 kV. X-ray photoelectron spectroscopy (XPS) data were acquired on an ESCALABMK II X-ray photoelectron spectrometer using Mg as the exciting source. The absorbance data of spectrophotometer were measured on SHIMADZU UV-1800 UV–vis spectrophotometer. The Brunauer–Emmett–Teller specific surface area (BET) was measured using a Micromeritics ASAP 2020. ^{1}H NMR spectra were collected on a superconducting-magnet NMR spectrometer (Bruker AVANCE III HD 500 MHz). The ion chromatography data were collected on 930 Compact IC Flex (Metrohm, Switzerland). The N_2 reduction experiments were carried out in a two-compartment H-type like electrolytic cell under ambient condition, which was separated by Nafion 117 membrane. The membrane was protonated by first boiling in ultrapure water for 1 h and treating in H_2O_2 (5%) aqueous solution at 80 °C for another 1 h, respectively. And then, the membrane was treaded in 0.5 M H_2SO_4 for 3 h at 80 °C and finally in water for 8 h. The electrochemical experiments were carried out with an electrochemical workstation (CHI 660E) using a three-electrode configuration. Mn_3O_4@rGO/CP was utilized as working

electrode for electrochemical N_2 reduction with the use of Ag/AgCl as the reference in the cathode chamber and graphite plate as the counter electrode in the anode chamber. The reference electrode was calibrated on RHE in this work with the following equation: E(RHE) = E(Ag/AgCl) + 0.61 V and the presented current density was normalized to the geometric surface area. For electrochemical N_2 reduction, all chrono-amperometry tests were performed in N_2-saturated 0.1 M Na_2SO_4 neutral solution (35 mL).

2.9 DFT calculation

To investigate the potential active sites of Mn_3O_4, DFT calculations were conducted using the Vienna ab initio simulation package (VASP) [37]. The spin-polarized DFT+U approach with U = 4.0 eV was applied to improve the description of the on-site Coulomb interactions of Mn (3d) electrons [38, 39]. The Projector Augmented Wave (PAW) potentials were applied to describe the electron-ion interactions [40]. The generalized gradient approximation (GGA) of Perdew–Burke–Ernzerhof (PBE) was used to calculate the electronic exchange-correction energy [41]. The cutoff energy of plane wave was set as 400 eV [42]. In all calculations, the convergence criteria for electronic energy were set as 10^{-4} eV and the criteria for force were set to be 0.05 eV·Å^{-1}. Three facets in bulk Mn_3O_4, (2 2 1), (1 1 2) and (1 0 3), were cleaved to study their interaction with N_2 molecule. A 3 × 3 × 3 Monkhorst–Pack k point sampling was adopted for the Brillouin zone integration. The thickness of vacuum layer in all calculations was set to be 15 Å. The binding energies between N_2 molecule and different surfaces were calculated with the DFT energies of each component as below

$$E_{\text{binding}} = E_{N_2+\text{surface}} - (E_{\text{surface}} + E_{N_2}) \quad (5)$$

where $E_{N_2+\text{surface}}$, E_{surface} and E_{N_2} are DFT energies of the model of N_2 on the cleaved surface, the pure surface and N_2 molecule, respectively.

3 Results and discussion

The XRD patterns of the rGO, pure Mn_3O_4 and Mn_3O_4@rGO are shown in Fig. 1(a). For rGO, diffraction peaks at 26.0° and 43.3° correspond to the (002) and (100) [43–45]. For pure Mn_3O_4, the peaks appear at 28.8°, 32.3°, 36.1°, 36.5°, 44.4°, 50.7°, 53.8°, 58.5°, 59.8°, and 64.6° corresponding to the (112), (103), (211), (202), (220), (105), (312), (321), (224), and (400) diffraction planes of Mn_3O_4 (JCPDS No. 46-1446). For XRD pattern of Mn_3O_4@rGO, the characteristic diffraction peaks are consistent with that of pure Mn_3O_4. Nevertheless, the diffraction peak of rGO at 26.0° and 43.3° cannot be clearly detected, which could be ascribed to the low stacking degree of rGO [46, 47]. To further investigate the structure of Mn_3O_4@rGO, the obtained Mn_3O_4@rGO is analyzed by Raman spectroscopy (Fig. 1(b)). Raman spectra display two strong absorption peaks with D (1,350 cm^{-1}) and G (1,598 cm^{-1}) peaks [48]. The intensity ratio of these two peaks (I_D/I_G) is calculated to be 1.01 for GO and 1.03 for Mn_3O_4@rGO, and the values of D and G peaks are listed in Table S1 in the Electronic Supplementary Material (ESM).

SEM image of Mn_3O_4@rGO (Fig. 1(c)) shows that their morphology is corrugated sheet feature [49]. A high-magnification SEM image (Fig. 1(c) inset) indicates that nanoparticles (dots) are adsorbed on the rGO. The SEM images of pure Mn_3O_4 and rGO are displayed in Fig. S1 in the ESM. Figure 1(d) exhibits the TEM image for Mn_3O_4@rGO. Clearly, a large amount of nanoparticles are decorated on the surface of rGO and the corresponding particles size distribution is shown in inset of Fig. 1(d). High-resolution TEM (HR-TEM) image (Fig. 1(e)) displays a well-resolved lattice fringe with an interplanar distance of 0.308 nm indexed to the (112) planes of Mn_3O_4@rGO. Figure S2 in the ESM shows the energy-dispersive X-ray (EDX) spectrum, confirming the presence of Mn, C, and O elements. EDX elemental mapping images of Mn_3O_4@rGO (Fig. 1(f)) reveal that the Mn, C, and O elements are uniformly distributed.

Figure 2(a) shows the XPS survey spectrum of Mn_3O_4@rGO, further indicating the presence of these three elements in product. As presented in Fig. 2(b), two peaks at 641.5 and 653.2 eV in the Mn 2p region agree with the binding energies (BEs) of Mn $2p_{3/2}$ and Mn $2p_{1/2}$, respectively. The spin–orbit splitting between Mn $2p_{3/2}$

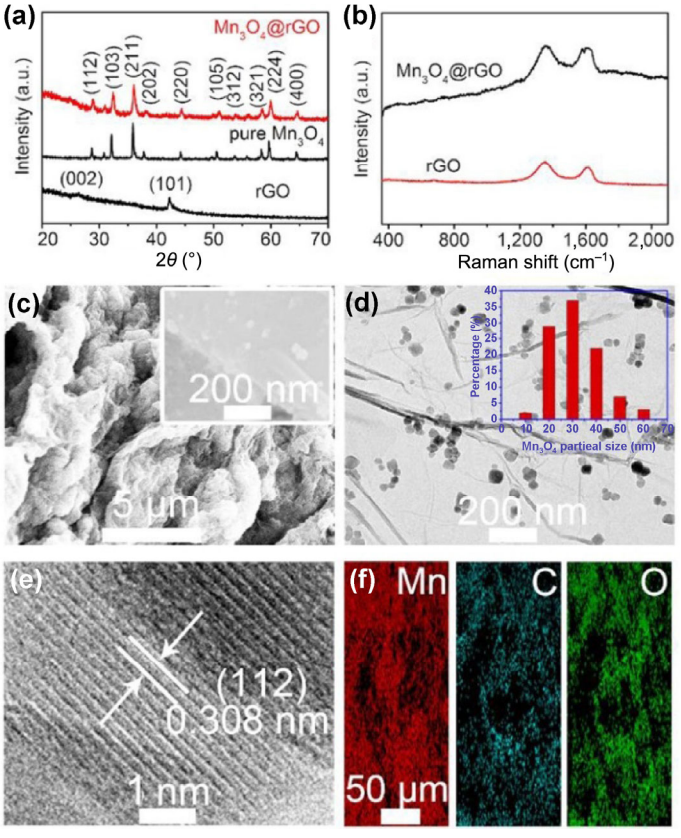

Figure 1 (a) XRD patterns of rGO, pure Mn_3O_4, and Mn_3O_4@rGO. (b) Raman spectra of rGO and Mn_3O_4@rGO. (c) SEM images of Mn_3O_4@rGO. (d) TEM (inset: particle size distribution histograms) and (e) HRTEM images taken from Mn_3O_4@rGO. (f) EDX elemental mapping images of Mn, C, and O elements for Mn_3O_4@rGO.

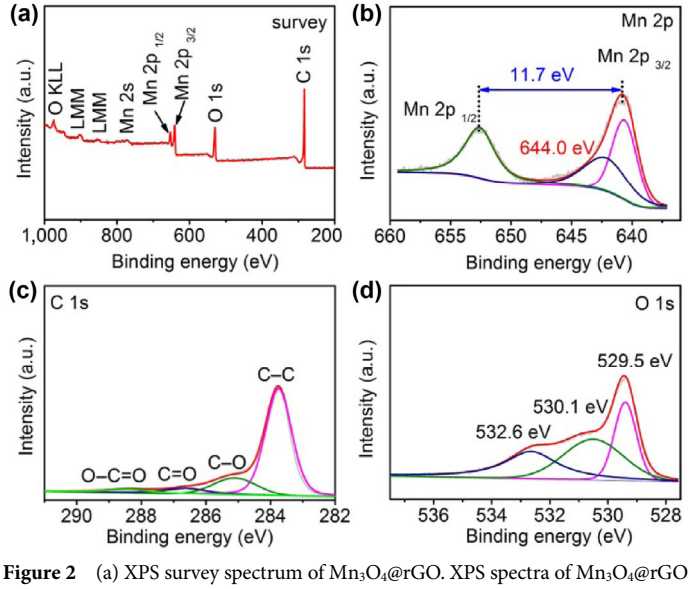

Figure 2 (a) XPS survey spectrum of Mn_3O_4@rGO. XPS spectra of Mn_3O_4@rGO in the (b) Mn 2p, (c) C 1s, and (d) O 1s regions.

and Mn $2p_{1/2}$ peaks is 11.7 eV, corresponding to the mixed valence Mn_3O_4 [50, 51]. The broadening at 644.0 eV is assigned to Mn $2p_{3/2}$ energy losses [52]. For C 1s XPS spectra (Fig. 2(c)), the peak is split into four signals. As observed, the peaks at 283.7, 285.7, 286.4, and 288.3 eV corresponds to C–C, C–O, C=O (epoxy and alkoxy), and O–C=O groups, respectively [53–55]. For O 1s XPS spectra (Fig. 2(d)), three different peaks centered at 529.5, 530.1, and 532.6 eV, which can verify the presence of Mn–O–C, Mn–O–Mn, and Mn–O–H bond, respectively [35].

NRR performance was tested in gas-tight two-compartment cell separated by a piece of Nafion 117 membrane. Mn_3O_4@rGO loaded on carbon paper (Mn_3O_4@rGO/CP, loading: 0.15 mg·cm^{-2}) was utilized as the working electrode. During the electrolysis process in 0.1 M Na_2SO_4, pure N_2 was continually bubbled to the Mn_3O_4@rGO cathode. All potentials were reported on a RHE scale. Both NH_3 and possible by-product hydrazine (N_2H_4) were spectrophotometrically evaluated and the calibration curves are shown in Figs. S3 and S4 in the ESM.

Time-dependent current density curves at various potentials under N_2 saturation are shown in Fig. 3(a), verifying electrocatalytic stability of this catalyst for NRR. Figure 3(b) displays the UV–vis absorption spectra of electrolyte coloured with indophenol indicator after 7,200 s electrlysis at given potentials. It is suggested that the electrocatalytic N_2 reduction process can be achieved at the corresponding potential. The NH_3 yields and corresponding FEs under different potentials are calculated and presented in Fig. 3(c). The maximum NH_3 yield of 17.4 μg·h^{-1}·mg$^{-1}_{cat.}$ with a highest FE of 3.52% can be obtained at −0.85 V. Notably, it compares favorably to the behaviors of most reported non-noble-metal NRR electrocatalysts (Table S2 in the ESM). Below the potential of –0.85 V, both NH_3 yields and FEs decrease significantly due to the competition of the hydrogen evolution reaction [56, 57]. Figure S5(a) displays the amount of H_2 determined by gas chromatography from the headspace of the cell in Ar- and N_2-saturated solutions at potentials from −0.75 to −0.95 V. Figure S5(b) details the selectivity of the catalyst in generating H_2 and NH_3 at given potentials in Ar- and N_2-saturated electrolytes. The unaccounted value may be attributed to the capacitance of the Mn_3O_4@rGO as well as dynamic H_2 adsorption and desorption on Mn_3O_4@rGO [58].

As shown in Fig. 3(d) and Fig. S6 in the ESM, we compared the FEs and corresponding NH_3 production after 2 hours electrolysis of different electrodes at −0.85 V. Clearly, bare carbon paper electrode has a poor NRR activity. In sharp contrast, Mn_3O_4@rGO electrode displays greatly enhanced NRR activity compared with pure Mn_3O_4 and rGO. The superior catalytic activity may be ascribed to the following aspects. (1) Nyquist plots (Fig. S7 in the ESM) suggest that Mn_3O_4@rGO has higher charge-transfer rate and thus faster NRR kinetics than that of pure Mn_3O_4 [53, 54]. Additionally, Fig. S8 shows current density curves of the Mn_3O_4 and Mn_3O_4@rGO in N_2-saturated 0.1 M Na_2SO_4 at −0.85 V, further proving that the introduction of rGO can significantly improve conductivity of the catalyst. (2) N_2 adsorption–desorption isotherms of Mn_3O_4@rGO and Mn_3O_4 (Fig. S9 in the ESM) suggest Mn_3O_4@rGO has a larger BET surface area of 151 m^2·g^{-1} than that of Mn_3O_4 (24 m^2·g^{-1}). (3) The double layer capacitances at the solid/liquid interface of Mn_3O_4@rGO, Mn_3O_4, and rGO are measured to be 10.8, 2.56, and 0.05 mF·cm^{-2}, respectively (Fig. S10 in the ESM), and the corresponding ECSAs are calculated to be 180, 43, and 0.8 cm^2, revealing much higher surface area with more exposed active sites for Mn_3O_4@rGO.

To confirm that the NH_3 is generated from NRR over Mn_3O_4@rGO, we tested Mn_3O_4@rGO/CP in N_2-saturated solution at open circuit potential, and Ar-saturated solution at −0.85 V. The results confirm that only N_2 provides the nitrogen source for NH_3 formation (Fig. 4(a)). The corresponding UV–vis absorption spectra are presented in Fig. S11 in the ESM. Additionally, the result of ^{15}N isotopic labeling experiment conducted confirms the source of N of NH_3 indeed come from N_2 rather than pollution (Fig. S12 in the ESM). We further performed electrolysis at −0.85 V with alternating 2 hours per cycles between Ar-saturated and N_2-saturated solution for 10 hours (Fig. 4(b)). The result also indicates that NH_3 only comes from N_2 [59]. To further verify the accuracy of results of the indophenol blue method, NH_4^+ produced in electrolyte was detected by ion chromatography. The results of ion chromatography (NH_3 yield: 16.6 μg·h^{-1}·mg$^{-1}_{cat.}$; FE: 3.34%) were close to the quantitative results from the indophenol blue method (Fig. S13 in the ESM). Moreover, no N_2H_4 was detected at each potential (Fig. S14 in the ESM), indicating the excellent selectivity of Mn_3O_4@rGO for NH_3 formation.

A stable performance is critical to the catalyst for NRR. Consecutive 24-hour electrolysis at −0.85 V only results in a slight decrease in current density, as shown in Fig. 4(c). Figure 4(d) displays consecutive recycling tests at −0.85 V for 5 times. Furthermore, the proportional relationship between NH_3 production and time indicates that NH_3 can be produced in at least 4 hours (Fig. S15 in the ESM). All these

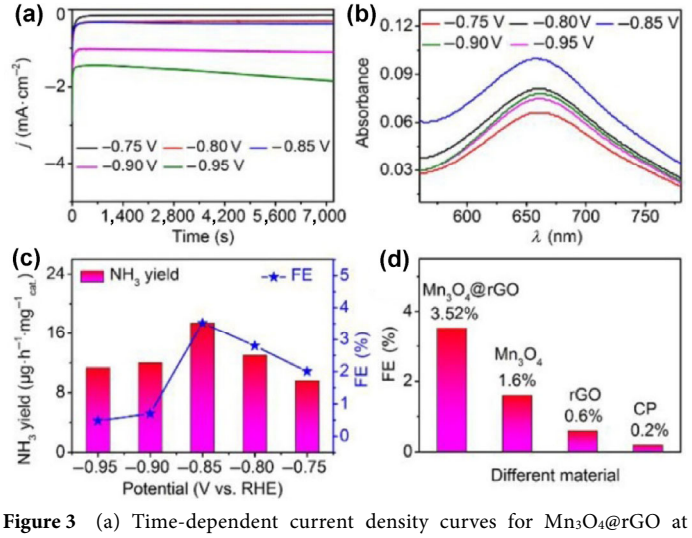

Figure 3 (a) Time-dependent current density curves for Mn_3O_4@rGO at different potentials in 0.1 M Na_2SO_4. (b) UV–vis absorption spectra of the electrolytes stained with indophenol indicator after electrolysis at a series of potentials for 7,200 s. (c) NH_3 yields and FEs at various potentials. (d) FE with different electrode at potential of −0.85 V.

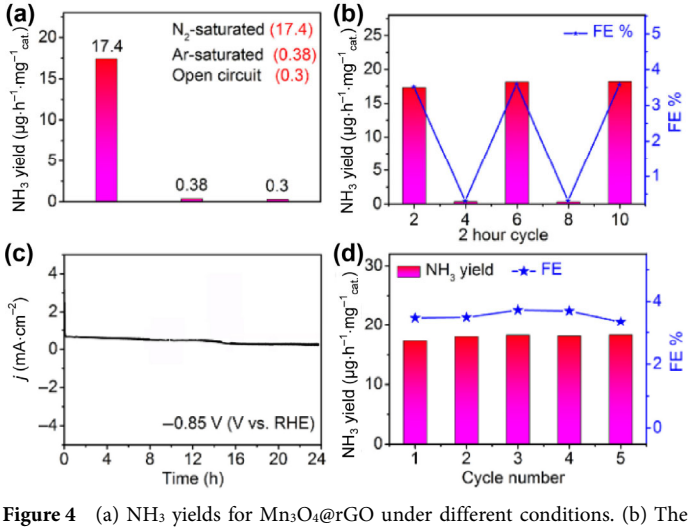

Figure 4 (a) NH_3 yields for Mn_3O_4@rGO under different conditions. (b) The NH_3 production rates and FEs of Mn_3O_4@rGO complex with alternating 2-hour cycles between N_2-saturated and Ar-saturated electrolytes. (c) Time-dependent current density curve for Mn_3O_4@rGO at potential of −0.85 V. (d) Recycling tests at −0.85 V under ambient conditions.

results indicate that such catalyst is extremely stable under the ambient conditions for NRR. With varying the N_2 flow rate, NH_3 yields and FEs at the potential of –0.85 V are also steady (Fig. S16 in the ESM), suggesting that the N_2 diffusion is a non-rate-determining step. Additionally, the XPS survey spectrum (Fig. S17 in the ESM) of Mn_3O_4@rGO after NRR test shows the unchanged peak positions indicating that electrochemical reduction did not change the chemical state of Mn_3O_4.

We conducted DFT calculation to study the active sites of Mn_3O_4. As presented in Fig. S18 in the ESM, the binding energies of N_2 molecule on (2 2 1), (1 1 2), and (1 0 3) surface were calculated to be –0.035, –0.32, and 0.29 eV, respectively. The calculated binding energies indicate that (2 2 1) surface has very weak absorption to N_2 molecule ($E_{binding}$ = –0.035 eV) and (1 0 3) surface even has no absorption to N_2 molecule ($E_{binding}$ = 0.29 eV). On the contrary, (1 1 2) surface exhibits decent absorption to N_2 molecule ($E_{binding}$ = –0.32 eV). The calculated binding energies agree well with the bonding length between N_2 molecule and the Mn atoms on different surfaces (Fig. S12 in the ESM): 2.70 Å on (2 2 1) surface, 2.14 Å on (1 1 2) surface and 4.40 Å on (1 0 3) surface.

4 Conclusions

In summary, Mn_3O_4@rGO is proved as an efficient electrocatalyst for NRR at ambient conditions. When tested in 0.1 M Na_2SO_4, such catalyst attains the NH_3 yield of 17.4 $\mu g \cdot h^{-1} \cdot mg^{-1}_{cat.}$ and the FE of 3.52% at –0.85 V vs. RHE, with high electrochemical stability and durability. This study would open up a new avenue for designing and developing carbon-based nanohybrids of Mn oxides [24, 60] and other metal oxide [61] with enhanced conductivity toward more efficient N_2 reduction electrocatalysis.

Acknowledgements

This work was supported by the National Natural Science Foundation of China (No. 21575137).

Electronic Supplementary Material: Supplementary material (SEM images, EDX and UV–vis absorption spectra, XPS spectrum, calibration and current density curves, Nyquist plots, CVs, Δj plotted vs. scan rates, NH_3 yields and FEs, NMR spectra, N_2 adsorption–desorption isotherms, ion chromatogram, calculated interaction, Tables S1 and S2) is available in the online version of this article at https://doi.org/10.1007/s12274-019-2352-5.

References

[1] Service, R. F. Chemistry. New recipe produces ammonia from air, water, and sunlight. *Science* **2014**, *345*, 610.

[2] Schlögl, R. Catalytic synthesis of ammonia—A "never-ending story"? *Angew. Chem., Int. Ed.* **2003**, *42*, 2004–2008.

[3] Smil, V. Detonator of the population explosion. *Nature* **1999**, *400*, 415.

[4] Rafiqul, I.; Weber, C.; Lehmann, B.; Voss, A. Energy efficiency improvements in ammonia production—Perspectives and uncertainties. *Energy* **2005**, *30*, 2487–2504.

[5] Jennings, J. R. *Catalytic Ammonia Synthesis: Fundamentals and Practice*; Spring: Boston, 1991.

[6] Chen, G. F.; Ren, S. Y.; Zhang, L. L.; Cheng, H.; Luo, Y. R.; Zhu, K. H.; Ding, L. X.; Wang, H. H. Advances in electrocatalytic N_2 reduction—Strategies to tackle the selectivity challenge. *Small Methods*, in press, DOI: 10.1002/smtd.201800337.

[7] Shipman, M. A.; Symes, M. D. Recent progress towards the electrosynthesis of ammonia from sustainable resources. *Catal. Today* **2017**, *286*, 57–68.

[8] Kyriakou, V.; Garagounis, I.; Vasileiou, E.; Vourros, A.; Stoukides, M. Progress in the electrochemical synthesis of ammonia. *Catal. Today* **2017**, *286*, 2–13.

[9] Bao, D.; Zhang, Q.; Meng, F. L.; Zhong, H. X.; Shi, M. M.; Zhang, Y.; Yan, J. M.; Jiang, Q.; Zhang, X. B. Electrochemical reduction of N_2 under ambient Conditions for artificial N_2 fixation and renewable energy storage using N_2/NH_3 cycle. *Adv. Mater.* **2017**, *29*, 1604799.

[10] Huang, H. H.; Xia, L.; Shi, X. F.; Asiri, A. M.; Sun, X. P. Ag nanosheets for efficient electrocatalytic N_2 fixation to NH_3 under ambient conditions. *Chem. Commun.* **2018**, *54*, 11427–11430.

[11] Liu, H. M.; Han, S. H.; Zhao, Y.; Zhu, Y. Y.; Tian, X. L.; Zeng, J. H.; Jiang, J. X.; Xia, B. Y.; Chen, Y. Surfactant-free atomically ultrathin rhodium nanosheet nanoassemblies for efficient nitrogen electroreduction. *J. Mater. Chem. A* **2018**, *6*, 3211–3217.

[12] Zhang, R.; Ren, X.; Shi, X. F.; Xie, F. Y.; Zheng, B. Z.; Guo, X. D.; Sun, X. P. Enabling effective electrocatalytic N_2 conversion to NH_3 by the TiO_2 nanosheets array under ambient conditions. *ACS Appl. Mater. Interfaces* **2018**, *10*, 28251–28255.

[13] Zhang, L.; Ren, X.; Luo, Y. L.; Shi, X. F.; Asiri, A. M.; Li, T. S.; Sun, X. P. Ambient NH_3 synthesis via electrochemical reduction of N_2 over cubic sub-micron SnO_2 particles. *Chem. Commun.* **2018**, ***54***, 12966–12969.

[14] Luo, Y. R.; Chen, G. F.; Ding, L.; Chen, X. Z.; Ding, L. X.; Wang, H. H. Efficient electrocatalytic N_2 fixation with MXene under ambient conditions. *Joule* **2019**, *3*, 279–289.

[15] Lv, C. D.; Yan, C. S.; Chen, G.; Ding, Y.; Sun, J. X.; Zhou, Y. S.; Yu, G. H. An amorphous noble-metal-free electrocatalyst that enables nitrogen fixation under ambient conditions. *Angew. Chem., Int. Ed.* **2018**, *57*, 6073–6076.

[16] Yang, D. S.; Chen, T.; Wang, Z. J. Electrochemical reduction of aqueous nitrogen (N_2) at a low overpotential on (110)-oriented Mo nanofilm. *J. Mater. Chem. A* **2017**, *5*, 18967–18971.

[17] Han, J. R.; Liu, Z. C.; Ma, Y. J.; Cui, G. W.; Xie, F. Y.; Wang, F. X.; Wu, Y. P.; Gao, S. Y.; Xu, Y. H.; Sun, X. P. Ambient N_2 fixation to NH_3 at ambient conditions: Using Nb_2O_5 nanofiber as a high-performance electrocatalyst. *Nano Energy* **2018**, *52*, 264–270.

[18] Li, X. H.; Li, T. S.; Ma, Y. J.; Wei, Q.; Qiu, W. B.; Guo, H. R.; Shi, X. F.; Zhang, P.; Asiri, A. M.; Chen, L. et al. Boosted electrocatalytic N_2 reduction to NH_3 by defect-rich MoS_2 nanoflower. *Adv. Energy Mater.* **2018**, *8*, 1801357.

[19] Zhu, X. J.; Liu, Z. C.; Liu, Q.; Luo, Y. L.; Shi, X. F.; Asiri, A. M.; Wu, Y. P.; Sun, X. P. Efficient and durable N_2 reduction electrocatalysis under ambient conditions: β-FeOOH nanorods as a non-noble-metal catalyst. *Chem. Commun.* **2018**, *54*, 11332−11335.

[20] Cheng, H.; Ding, L. X.; Chen, G. F.; Zhang, L. L.; Xue, J.; Wang, H. H. Molybdenum carbide nanodots enable efficient electrocatalytic nitrogen fixation under ambient conditions. *Adv. Mater.* **2018**, *30*, 1803694.

[21] Zhang, Y.; Qiu, W. B.; Ma, Y. J.; Luo, Y. L.; Tian, Z. Q.; Cui, G. W.; Xie, F. Y.; Chen, L.; Li, T. S.; Sun, X. P. High-performance electrohydrogenation of N_2 to NH_3 catalyzed by multishelled hollow Cr_2O_3 microspheres under ambient conditions. *ACS Catal.* **2018**, *8*, 8540–8544.

[22] Zhao, J. X.; Zhang, L.; Xie, X. Y.; Li, X. H.; Ma, Y. J.; Liu, Q.; Fang, W. H.; Shi, X. F.; Cui, G. L.; Sun, X. P. Ti_3C_2Tx (T = F, OH) MXene nanosheets: Conductive 2D catalysts for ambient electrohydrogenation of N_2 to NH_3. *J. Mater. Chem. A* **2018**, *6*, 24031–24035.

[23] Chen, G. F.; Cao, X. R.; Wu, S. Q.; Zeng, X. Y.; Ding, L. X.; Zhu, M.; Wang, H. H. Ammonia electrosynthesis with high selectivity under ambient conditions via a Li^+ incorporation strategy. *J. Am. Chem. Soc.* **2017**, *139*, 9771–9774.

[24] Wu, X. F.; Xia, L.; Wang, Y.; Lu, W. B.; Liu, Q.; Shi, X. F.; Sun, X. P. Mn_3O_4 nanocube: An efficient electrocatalyst toward artificial N_2 fixation to NH_3. *Small* **2018**, *14*, 1803111.

[25] Wang, H. L.; Cui, L. F.; Yang, Y.; Casalongue, H. S.; Robinson, J. T.; Liang, Y. Y.; Cui, Y.; Dai, H. J. Mn_3O_4-graphene hybrid as a high-capacity anode material for lithium ion batteries. *J. Am. Chem. Soc.* **2010**, *132*, 13978–13980.

[26] Di Blasi, A.; Busaccaa, C.; Di Blasia, O.; Briguglioa, N.; Squadritoa, G.; Antonuccia, V. Synthesis of flexible electrodes based on electrospun carbon nanofibers with Mn_3O_4 nanoparticles for vanadium redox flow battery application. *Appl. Energy* **2017**, *190*, 165–171.

[27] Qu, L. T.; Liu, Y.; Baek, J. B.; Dai, L. M. Nitrogen-doped graphene as efficient metal-free electrocatalyst for oxygen reduction in fuel cells. *ACS Nano* **2010**, *4*, 1321–1326.

[28] Xing, Z. C.; Chu, Q. X.; Ren, X. B.; Tian, J. Q.; Asiri, A. M.; Alamry, K. A.; Al-Youbi, A. O.; Sun, X. P. Biomolecule-assisted synthesis of nickel sulfides/reduced graphene oxide nanocomposites as electrode materials for supercapacitors. *Electrochem. Commun.* **2013**, *32*, 9–13.

[29] Yang, S. B.; Zhi, L. J.; Tang, K.; Feng, X. L.; Maier, J.; Müllen, K.

Efficient synthesis of heteroatom (N or S)-doped graphene based on ultrathin graphene oxide-porous silica sheets for oxygen reduction reactions. *Adv. Funct. Mater.* **2012**, *22*, 3634–3640.

[30] Stankovich, S.; Dikin, D. A.; Dommett, G. H. B.; Kohlhaas, K. M.; Zimney, E. J.; Stach, E. A.; Piner, R. D.; Nguyen S. T.; Ruoff, R. S. Graphene-based composite materials. *Nature* **2006**, *442*, 282–286.

[31] Wang, J. G.; Jin, D. D.; Zhou, R.; Li, X.; Liu, X. R.; Shen, C.; Xie, K. Y.; Li, B. H.; Kang, F. Y.; Wei, B. Q. Highly flexible graphene/Mn_3O_4 nanocomposite membrane as advanced anodes for li-ion batteries. *ACS Nano* **2016**, *10*, 6227−6234.

[32] Zhang, X. X.; Liu, Q.; Shi, X. F.; Asiri, A. M.; Luo, Y. L.; Sun, X. P.; Li, T. S. TiO_2 nanoparticles-reduced graphene oxide hybrid: An efficient and durable electrocatalyst toward artificial N_2 fixation to NH_3 under ambient conditions. *J. Mater. Chem. A* **2018**, *6*, 17303–17306.

[33] Kibsgaard, J.; Tsai, C.; Chan, K. R.; Benck, J. D.; Nørskov, J. K.; Abild-Pedersen, F.; Jaramillo, T. F. Designing an improved transition metal phosphide catalyst for hydrogen evolution using experimental and theoretical trends. *Energy Environ. Sci.* **2015**, *8*, 3022–3029.

[34] Popczun, E. J.; McKone, J. R.; Read, C. G.; Biacchi, A. J.; Wiltrout, A. M.; Lewis, N. S.; Schaak, R. E. Nanostructured nickel phosphide as an electrocatalyst for the hydrogen evolution reaction. *J. Am. Chem. Soc.* **2013**, *135*, 9267–9270.

[35] Zhu, D.; Zhang, L. H.; Ruther, R. E.; Hamers, R. J. Photo-illuminated diamond as a solid-state source of solvated electrons in water for nitrogen reduction. *Nat. Mater.* **2013**, *12*, 836–841.

[36] Watt, G. W.; Chrisp, J. D. A spectrophotometric method for the determination of hydrazine. *Anal. Chem.* **1952**, *24*, 2006–2008.

[37] Segall, M. D.; Linda, P. J. D.; Probert, M. J.; Pickard, C. J.; Hasnip, P. J.; Clark, S. J.; Payne, M. C. First-principles simulation: Ideas, illustrations and the CASTEP code. *J. Phys. Condens. Matter* **2002**, *14*, 2717–2744.

[38] Jain, A.; Hautier, G.; Ong, S. P.; Moore, C. J.; Fischer, C. C.; Persson, K. A.; Ceder, G. Formation enthalpies by mixing GGA and GGA + U calculations. *Phys. Rev. B* **2011**, *84*, 045115.

[39] Wang, L.; Maxisch, T.; Ceder, G. Oxidation energies of transition metal oxides within the GGA + U framework. *Phys. Rev. B* **2006**, *73*, 195107.

[40] Kresse, G.; Furthmüller, J. Efficient iterative schemes for *ab initio* total-energy calculations using a plane-wave basis set. *Phys. Rev. B* **1996**, *54*, 11169–11186.

[41] Perdew, J. P.; Chevary, J. A.; Vosko, S. H.; Jackson, K. A.; Pederson, M. R.; Singh, D. J.; Fiolhais, C. Atoms, molecules, solids, and surfaces: Applications of the generalized gradient approximation for exchange and correlation. *Phys. Rev. B* **1992**, *46*, 6671–6687.

[42] Gong, F.; Ding, Z. W.; Fang, Y.; Tong, C. J.; Xia, D. W.; Lv, Y. Y.; Wang, B.; Papavassiliou, D. V.; Liao, J. X.; Wu, M. Q. Enhanced electrochemical and thermal transport properties of graphene/MoS_2 heterostructures for energy storage: Insights from multiscale modeling. *ACS Appl. Mater. Interfaces* **2018**, *10*, 14614–14621.

[43] Zhang, G. G.; Kong, M. L.; Yao, Y. D.; Long, L.; Yan, M. L.; Liao, X. M.; Yin, G. F.; Huang, Z. B.; Asiri, A. M.; Sun, X. P. One-pot synthesis of γ-MnS/reduced graphene oxide with enhanced performance for aqueous asymmetric supercapacitors. *Nanotechnology* **2017**, *28*, 065402.

[44] Tang, L. H.; Wang, Y.; Li, Y. M.; Feng, H. B.; Lu J.; Li, J. H. Preparation, structure, and electrochemical properties of reduced graphene sheet films. *Adv. Funct. Mater.* **2009**, *19*, 2782–2789.

[45] Liu, X. J.; Pan, L. K.; Lv, T.; Zhu, G.; Sun, Z.; Sun, C. Q. Microwave-assisted synthesis of CdS-reduced graphene oxide composites for photocatalytic reduction of Cr (VI). *Chem. Commun.* **2011**, *47*, 11984–11986.

[46] Yang, S. H.; Song, X. F.; Zhang, P.; Gao, L. Crumpled nitrogen-doped graphene–ultrafine Mn_3O_4 nanohybrids and their application in supercapacitors. *J. Mater. Chem. A* **2013**, *1*, 14162–14169.

[47] Liu, C. L.; Chang, K. H.; Hu, C. C.; Wen, W. C. Microwave-assisted hydrothermal synthesis of Mn_3O_4/reduced graphene oxide composites for high power supercapacitors. *J. Power Sources* **2012**, *217*, 184–192.

[48] Wang, H. L.; Hao, Q. L.; Yang, X. J.; Lu, L. D.; Wang, X. A nanostructured graphene/polyaniline hybrid material for supercapacitors. *Nanoscale* **2010**, *2*, 2164–2170.

[49] Zhang, L. S.; Zhao, L. J.; Lian, J. S. Nanostructured Mn_3O_4–reduced graphene oxide hybrid and its applications for efficient catalytic decomposition of orange II and high lithium storage capacity. *RSC Adv.* **2014**, *4*, 41838–41847.

[50] Wang, C. B.; Yin, L. W.; Xiang, D.; Qi, Y. X. Uniform carbon layer coated Mn_3O_4 nanorod anodes with improved reversible capacity and cyclic stability for lithium ion batteries. *ACS Appl. Mater. Interfaces* **2012**, *4*, 1636−1642.

[51] Bag, S.; Roy, K.; Gopinath, C. S.; Raj, C. R. Facile single-step synthesis of nitrogen-doped reduced graphene oxide-Mn_3O_4 hybrid functional material for the electrocatalytic reduction of oxygen. *ACS Appl. Mater. Interfaces* **2014**, *6*, 2692–2699.

[52] Liu, T. T.; Ma, X.; Liu, D. N.; Hao, S.; Du, G.; Ma, Y. J.; Asiri, A. M.; Sun, X. P.; Chen, L. Mn doping of CoP nanosheets array: An efficient electrocatalyst for hydrogen evolution reaction with enhanced activity at all pH values. *ACS Catal.* **2017**, *7*, 98–102.

[53] Wu, Y. Z.; Liu, S. Q.; Wang, H. Y.; Wang, X. W.; Zhang, X.; Jin, G. H. A novel solvothermal synthesis of Mn_3O_4/graphene composites for supercapacitors. *Electrochim. Acta* **2013**, *90*, 210–218.

[54] Lee, J. W.; Hall, A. S.; Kim, J. D.; Mallouk, T. E. A facile and template-free hydrothermal synthesis of Mn_3O_4 nanorods on graphene sheets for supercapacitor electrodes with long cycle stability. *Chem. Mater.* **2012**, *24*, 1158–1164.

[55] Tian, Y. Y.; Li, D. W.; Liu, J. L.; Wang, H.; Zhang, J. F.; Zheng, Y. Q.; Liu, T. H.; Hou, S. F. Facile synthesis of Mn_3O_4 nanoplates-anchored graphene microspheres and their applications for supercapacitors. *Electrochim. Acta* **2017**, *257*, 155–164.

[56] Ren, X.; Zhao, J. X.; Wei, Q.; Ma, Y. J.; Guo, H. R.; Liu, Q.; Wang, Y.; Cui, G. W.; Asiri, A. M.; Li, B. H. et al. High-performance N_2-to-NH_3 conversion electrocatalyzed by Mo_2C nanorod. *ACS Cent. Sci.* **2018**, *5*, 116–121.

[57] Qiu, W. B.; Xie, X. Y.; Qiu, J. D.; Fang, W. H.; Liang, R. P.; Ren, X.; Ji, X. Q.; Cui, G. W.; Asiri, A. M.; Cui, G. L. et al. High-performance artificial nitrogen fixation at ambient conditions using a metal-free electrocatalyst. *Nat. Commun.* **2018**, *9*, 3485.

[58] Wang, J.; Yu, L.; Hu, L.; Chen, G.; Xin, H. L.; Feng, X. F. Ambient ammonia synthesis via palladium-catalyzed electrohydrogenation of dinitrogen at low overpotential. *Nat. Commun.* **2018**, *9*, 1795.

[59] Zhang, Y.; Du, H.; Ma, Y.; Ji, L.; Guo, H.; Tian, Z.; Chen, H.; Huang, H.; Cui, G.; Asiri, A. M. et al. Hexagonal boron nitride nanosheet for effective ambient N_2 fixation to NH_3. *Nano Res.* **2019**, *12*, 919–924.

[60] Wang, Z.; Gong, F.; Zhang, L.; Wang, R.; Ji, L.; Liu, Q.; Luo, Y. L.; Guo, H. R.; Li, Y. H.; Gao, P. et al. Electrocatalytic hydrogenation of N_2 to NH_3 by MnO: Experimental and theoretical investigations. *Adv. Sci.* **2019**, *6*, 1801182.

[61] Zhu, Y. Q.; Cao, T.; Li, Z.; Chen, C.; Peng, Q.; Wang, D. S.; Li, Y. D. Two-dimensional SnO_2/graphene heterostructures for highly reversible electrochemical lithium storage. *Sci. China Mater.* **2018**, *61*, 1527–1535.